JGR Planets

Key Points:

- Ultraviolet reflected sunlight observations from Juno Ultraviolet Spectrograph were used to study the C_2H_2 abundance in Jupiter's stratosphere
- The stratospheric C_2H_2 abundance decreases at high latitudes, in agreement with previous studies using infrared data
- The latitudinal distribution of C_2H_2 can be used to constrain horizontal mixing rates

Supporting Information:

Supporting Information may be found in the online version of this article.

Correspondence to:

R. S. Giles,
rgiles@swri.edu

Meridional Variations of C_2H_2 in Jupiter's Stratosphere From Juno UVS Observations

Rohini S. Giles[1] , **Thomas K. Greathouse**[1] , **Vincent Hue**[1] ,
G. Randall Gladstone[1,2] , **Henrik Melin**[3] , **Leigh N. Fletcher**[3] , **Patrick G. J. Irwin**[4],
Joshua A. Kammer[1] , **Maarten H. Versteeg**[1] , **Bertrand Bonfond**[5] , **Denis C. Grodent**[5],
Scott J. Bolton[1] , and **Steven M. Levin**[6]

[1]Space Science and Engineering Division, Southwest Research Institute, San Antonio, TX, USA, [2]Department of Physics and Astronomy, University of Texas at San Antonio, San Antonio, TX, USA, [3]School of Physics & Astronomy, University of Leicester, Leicester, UK, [4]Department of Physics, University of Oxford, Oxford, UK, [5]Laboratoire de Physique Atmosphérique et Planétaire, STAR Institute, Université de Liège, Liège, Belgium, [6]Jet Propulsion Laboratory, Pasadena, CA, USA

Abstract The Ultraviolet Spectrograph (UVS) instrument on the Juno mission records far-ultraviolet reflected sunlight from Jupiter. These spectra are sensitive to the abundances of chemical species in the upper atmosphere and to the distribution of the stratospheric haze layer. We combine observations from the first 30 perijoves of the mission in order to study the meridional distribution of acetylene (C_2H_2) in Jupiter's stratosphere. We find that the abundance of C_2H_2 decreases toward the poles by a factor of 2–4, in agreement with previous analyses of mid-infrared spectra. This result is expected from insolation rates: near the equator, the UV solar flux is higher, allowing more C_2H_2 to be generated from the UV photolysis of CH_4. The decrease in abundance toward the poles suggests that horizontal mixing rates are not rapid enough to homogenize the latitudinal distribution.

Plain Language Summary The Ultraviolet Spectrograph instrument on the Juno mission to Jupiter is primarily used to study the planet's ultraviolet auroras, but also records reflected sunlight from the planet's upper atmosphere. These ultraviolet reflected sunlight observations can be used to measure the abundances of different gases in Jupiter's stratosphere. In this study, we focus on one prominent molecule, acetylene, and study how its abundance varies with latitude. We find that its abundance decreases toward Jupiter's poles, which agrees with previous results obtained from studying the same molecule with infrared observations.

1. Introduction

Hydrocarbons play a significant role in Jupiter's stratosphere. Methane (CH_4) is the most abundant spectro-scopically absorbing gas in the stratosphere and its photolysis by UV photons leads to a rich hydrocarbon photochemistry (Moses et al., 2004). The most abundant products of CH_4 photolysis are ethane (C_2H_6) and acetylene (C_2H_2), the latter of which is the focus of this study. C_2H_6 and C_2H_2 were first detected in Jupiter's stratosphere by Ridgway (1974) using ground-based observations at 10 μm, and this was followed by the subsequent detections of other hydrocarbons including C_2H_4, C_3H_4, and C_6H_6 (Kim et al., 1985).

As disequilibrium species, these hydrocarbons act as tracers of the atmospheric circulation and chemistry in Jupiter's stratosphere. Spatial variability in the abundance of a given disequilibrium species can provide valuable constraints in understanding how production rates and mixing rates vary across the planet. Non-auroral latitudinal variations can provide information about horizontal eddy diffusion rates (Hue et al., 2018; Lellouch et al., 2006; Nixon et al., 2007), while spatial variability within the auroral region can tell us about auroral dynamics and enhanced ion-related chemistry due to auroral precipitation (Sinclair et al., 2019, 2020; Wong et al., 2000).

The focus of this study is latitudinal variations in C_2H_2 outside of the auroral regions. Since its first detection by Ridgway (1974), numerous studies have constrained Jupiter's stratospheric C_2H_2 abundance using observations from both the infrared (e.g., Drossart et al., 1986; Fouchet et al., 2000; Sada et al., 1998) and the ultraviolet (e.g., Gladstone & Yung, 1983). The first spatially-resolved full-planet retrievals of C_2H_2 abundance

were carried out by Kunde et al. (2004) and Nixon et al. (2007), using infrared observations from the Cassini CIRS instrument, and similar analyses were later carried out using Voyager data (Nixon et al., 2010; Zhang, Nixon, et al., 2013). Nixon et al. (2007) found that the 5-mbar C_2H_2 abundance peaked at 20°N and then decreased toward the poles by a factor of ∼4. Similar latitudinal trends have also been observed using ground-based mid-infrared spectroscopic observations (Fletcher et al., 2016; Melin et al., 2018).

As discussed in Nixon et al. (2007), a decrease in C_2H_2 abundance toward the poles can be understood by considering the lifetime of C_2H_2 in Jupiter's stratosphere. At 5 mbar, C_2H_2 has a chemical lifetime of 3×10^7 s, which is shorter than the expected horizontal mixing timescales of >1 Jovian year (4×10^8 s). The incident UV flux is greater at the equator than at high latitudes, causing more C_2H_2 to be produced at low latitudes and the short lifetime means that it is not transported to the poles rapidly enough to homogenize the latitudinal distribution. Assuming that the C_2H_2 chemistry is well known, its meridional distribution can therefore be used to constrain the horizontal mixing timescale and a comparison of the meridional distribution at different pressure levels can constrain how the horizontal mixing changes with altitude.

In this study, we present the first full-planet meridional retrievals of C_2H_2 from ultraviolet reflected sunlight observations of Jupiter, using data from the Ultraviolet Spectrograph (UVS) instrument on the Juno spacecraft. This builds on previous work from Melin et al. (2020) who retrieved low-latitude abundances from Cassini UVIS data, which have a lower spatial resolution but higher spectral resolution than the Juno UVS observations. In Section 2, we describe the observations made with the UVS instrument on the Juno spacecraft. In Section 3, we describe the meridional retrieval of the stratospheric C_2H_2 abundance and in Section 4, we compare this distribution with previous meridional distributions from infrared observations.

2. Observations

2.1. Juno UVS

The UVS instrument (Gladstone et al., 2017) is a far-ultraviolet imaging spectrograph on NASA's Juno mission, which arrived at Jupiter in July 2016 and is currently in a highly elliptical 53-day polar orbit around the planet (Bolton et al., 2017). Observations of Jupiter are obtained for several hours on either side of each perijove (PJ), the closest point of approach in the orbit. The primary scientific goal of UVS is to study Jupiter's auroral emissions and the instrument's spectral range of 68–210 nm was designed to cover several important H and H_2 emission bands. However, the longer wavelengths covered by UVS extend into a spectral region that is dominated by reflected sunlight; this part of the spectrum is sensitive to hydrocarbons and aerosols (Gladstone et al., 2017) and will be the focus of this study. At >200 nm, the UVS sensitivity drops off significantly, increasing the uncertainty on the radiometric calibration. In this study, we focus on the 164–200 nm segment of the spectrum. At these wavelengths, ultraviolet reflected photons are primarily reflected from the 5–50 mbar pressure level (Melin et al., 2020) and the spectrum is therefore sensitive to molecular absorbers in this region of the atmosphere or higher.

UVS has a dog-bone shaped slit with a total length of 7.2°. The outer wide segments of the slit have a spectral resolution of 2–3 nm and the central narrow segment has a spectral resolution of ∼1.3 nm. In this study, we only use data from the wide segments of the slit, as the signal-to-noise ratio is significantly better. As the Juno spacecraft spins with a period of ∼30 s, the field-of-view defined by the UVS slit sweeps across a swath of Jupiter. Ultraviolet photon detections are recorded in a pixel-list format, containing information about the wavelength of the photon, the position along the slit, and the precise time of the detection. The position along the slit can be combined with information about the orientation of the spacecraft at the time of observation in order to map the photon to a latitude and longitude on the planet. This allows spectral image cubes of the planet to be built up.

2.2. Reflected Sunlight Spectra

As Juno is in a polar orbit around Jupiter, the majority of the UVS observations cover Jupiter's polar regions. An analysis of the UVS reflected sunlight observations of Jupiter's poles will be the focus of a future study; in this study, we focus on meridional trends and limit our analysis to regions of the planet without auroral
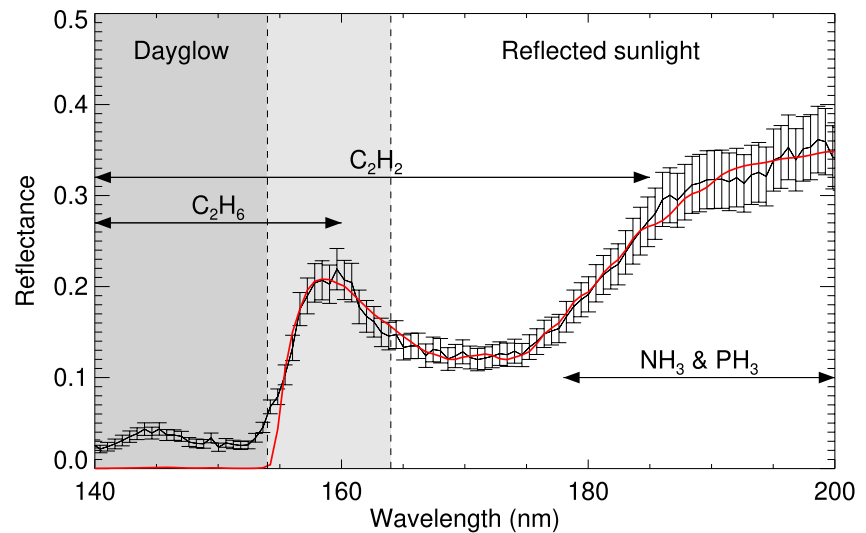
Figure 1. Jupiter's equatorial reflectance spectrum (corrected for the solar zenith angle) observed by Juno's Ultraviolet Spectrograph (black) alongside the best-fit model NEMESIS spectrum (red). The primary molecular absorber in this spectral range is C_2H_2 but there are also smaller contributions from C_2H_6, NH_3, and PH_3. At <154 nm, the spectrum is dominated by dayglow and at >164 nm, the spectrum is dominated by reflected sunlight. In this study, we focus on the 164–200 nm segment of the UVS spectrum.

emissions, which extend into the reflected sunlight part of the spectrum and complicate radiative transfer modeling.

In order to obtain sufficient signal-to-noise at all latitudes, we combine wide-slit dayside observations from the first 30 perijoves of the mission (August 2016–November 2020) and bin them into 10°-wide latitude bins. We use all data from the main perijove observing sequence, which is typically ±5 h from the time of closest approach. In order to avoid the auroral regions of the planet, we exclude longitudes and latitudes that fall poleward of a boundary oval, set at 5,000 km equatorward of the Io footprint reference oval (Bonfond et al., 2017). Figure S1 shows maps of these excluded auroral regions.

For the combined observations in each latitude bin, we produce a 2-dimensional histogram of emission angle and solar zenith angle in order to determine the geometric coverage. Figure S2 shows these histograms for two example latitude bins. In order to easily compare different latitudes, we looked for a combination of angles that were available at all latitudes. We found that all latitude bins included observations obtained with an emission angle of 40–50° and a solar zenith angle of 70–80°; this combination is shown by the red boxes in Figure S2. For each latitude bin, data fulfilling these angle criteria were averaged together, producing a set of representative spectra at each latitude, each with a comparable observing geometry. These representative spectra combine observations from many perijoves.

An example Juno UVS spectrum from the latitude bin centered on the equator is shown in black in Figure 1. This spectrum is shown in terms of the planet's reflectance, i.e., the observed spectrum has been divided by the incident solar spectrum, corrected for the solar zenith angle. UVS observations have background radiation noise due to the penetrating high-energy electrons in the environment around Jupiter (Kammer et al., 2019). We estimate the radiation noise level from the average count rate at <80 nm (where we expect the counts to all be due to radiation) and this has been subtracted from the spectrum. The error bars are calculated by adding in quadrature the radiation noise and the shot noise (a signal-to-noise ratio of $\sqrt{N}$, where N is the number of photon counts recorded before radiation noise subtraction). The red line in Figure 1 shows the best-fit model reflected sunlight spectrum obtained with the NEMESIS radiative transfer and retrieval tool and is discussed in Section 3.

At <154 nm, the Jovian spectrum is dominated by the H_2 Lyman band emission from dayglow, rather than reflected sunlight (Morrissey et al., 1995). At 154–164 nm, both dayglow and reflected sunlight contribute to the shape of the spectrum and by >164 nm, reflected sunlight is the dominant component. The dominant
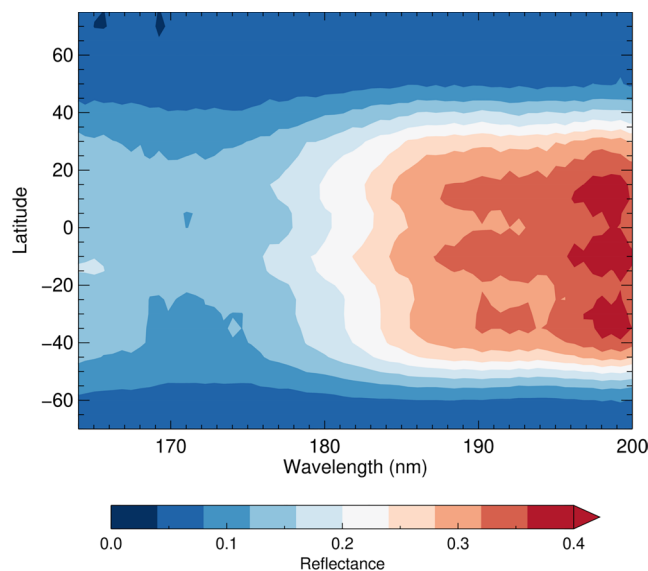
Figure 2. Contour plot of reflected sunlight spectra (corrected for the solar zenith angles) as a function of latitude, from Juno's Ultraviolet Spectrograph. At high latitudes, the average reflectance is lower and the spectra are flatter.

stratospheric species that affects the spectral shape in the 140–200 nm wavelength range is C_2H_2, which is the focus of this study. C_2H_2 has a peak in absorption at ~172 nm, causing the broad dip seen in Figure 1. The sharp drop at the short-wavelength edge of the spectrum is primarily due to C_2H_6 absorption, although C_2H_2 also plays a role. The peak at 160 nm is primarily caused by the absorption cross-section of these two gases, although there is also a peak in the H_2 dayglow emission at this wavelength which can further increase the radiance. Due to this, we restrict our radiative transfer modeling in the following sections to the 164–200 nm segment of the UVS spectrum.

C_2H_4 and C_4H_2 also absorb light in this part of the ultraviolet spectrum, but at the abundances in which they are present in the stratosphere, their impact on the spectral shape is minor. The other two absorbing species of note are NH_3 and PH_3; these gases are not normally present in Jupiter's stratosphere, although stratospheric NH_3 was observed in the aftermath of the Shoemaker-Levy 9 impact on Jupiter (Kostiuk et al., 1996) and the 2009 impactor (Fletcher et al., 2011). However, their presence in the upper troposphere can affect the spectral shape, particularly at the longer wavelengths where there is less absorption from stratospheric species. Forward models showing the individual impacts of these molecular species are presented in Melin et al. (2020).

Figure 1 showed an example spectrum from the latitude bin centered on Jupiter's equator. Inspection of the spectra from all latitude bins shows that the spectra vary considerably. First, the average reflectance decreases toward the poles, which is due to the increasing opacity of the stratospheric haze. In addition to the average reflectance changing, we also find that the spectral shape at 164–200 nm changes. These effects are shown in Figure 2, which presents a contour plot of the spectra as a function of latitude. At higher latitudes, Figure 2 shows a lower average reflectance. These high-latitude spectra are also relatively flat across the entire 164–200 nm spectral range, while spectra from near the equator show a broad minimum at ~172 nm. As C_2H_2 has a peak in its absorption cross-section at ~172 nm, this suggests that the variability in spectral shape could be due to decreasing C_2H_2 abundance at high latitudes. This is explored using a radiative transfer and retrieval code in Section 3.

3. Analysis

3.1. Radiative Transfer and Retrieval Code

In order to determine the C_2H_2 abundance as a function of latitude, we analyzed the Juno UVS spectra using the NEMESIS radiative transfer and retrieval tool (Irwin et al., 2008). NEMESIS was originally developed in order to analyze infrared observations from Cassini CIRS, but was later expanded to cover visible and sub-mm wavelengths and has been applied to a wide range of ground-based and spacecraft observations. More recently, Melin et al. (2020) extended these capabilities into the ultraviolet in order to model Cassini UVIS observations at 150–190 nm.

At wavelengths >164 nm, Jupiter's spectrum is dominated by Rayleigh-scattered sunlight. NEMESIS calculates multiple scattering by using a matrix operator approach (Plass et al., 1973). This scattered sunlight is absorbed by molecules in Jupiter's atmosphere, such as C_2H_2. Light can also be absorbed and/or scattered by aerosols in Jupiter's atmosphere. For a given set of vertical temperature, abundance, and aerosol profiles, viewing geometry and incident solar spectrum, NEMESIS calculates a synthetic top-of-atmosphere spectrum. This synthetic spectrum is compared to the observed spectrum and the atmospheric profiles are iteratively adjusted to fit the observed spectrum, following an optimal estimation approach (Rodgers, 2000). The final fit minimizes the chi-square statistic between the observations and the model, taking into account both the noise on the observations and an estimated 10% error in the radiative transfer calculations.

Raman scattering, in which photons are scattered inelastically, is not currently included in NEMESIS. At wavelengths greater than 210 nm, Raman scattering can have a significant impact on the reflectance
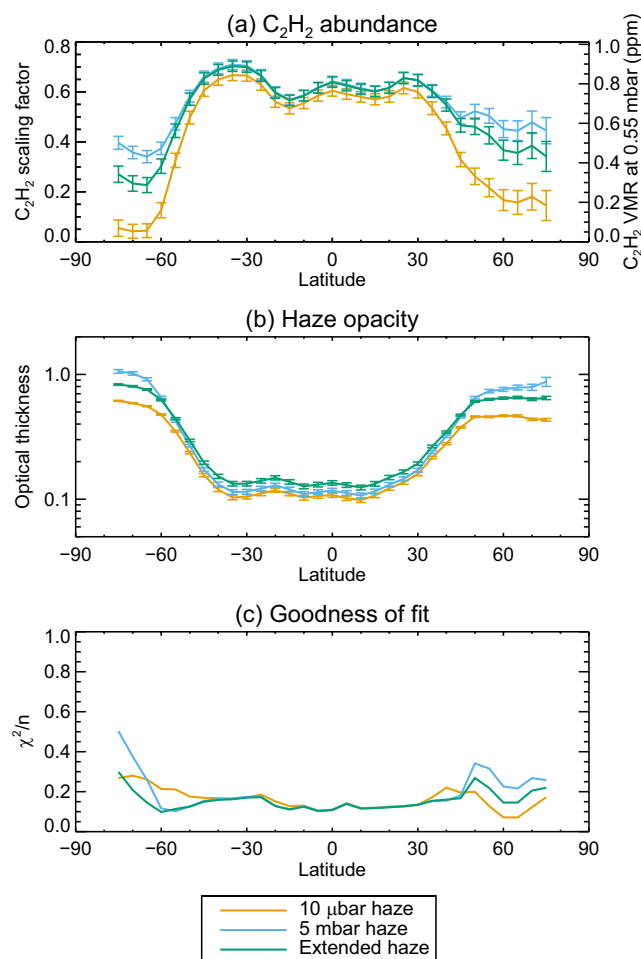
Figure 3. The results of the latitudinal retrievals for three different cloud models. Panel (a) shows the retrieved C_2H_2 abundance as a function of latitude. The left axis shows the abundance in terms of the retrieved scaling factor relative to Model C in Moses et al. (2005) and the right axis shows how this scaling factor converts into a relative abundance at 5 mbar. Panel (b) shows the retrieved haze opacity and panel (c) shows the reduced chi-square statistic.

spectrum, contributing 3–6% to the continuum and producing multiple identifiable spectral features (Bétremieux & Yelle, 1999). In contrast, at less than 210 nm, Raman scattering does not produce clear spectral features and contributes 2–3% to the continuum. This is a similar size to the noise on the observations, and forms part of the assumed 10% error in the radiative transfer calculations.

In this study, we use the atmosphere "Model C" described in Moses et al. (2005) as the a priori atmospheric model. In some retrievals, we also include NH_3 and PH_3, which are not present in the stratosphere-focused Model C. The a priori NH_3 and PH_3 vertical profiles are obtained from Cassini CIRS observations (Fletcher et al., 2016) and assume an abundance of zero above the tropopause. The sources of ultraviolet absorption cross-sections and the solar spectrum are described in Melin et al. (2020) and both were smoothed to match the spectral resolution of the Juno UVS wide slit. For simplicity, we assume that the aerosols in the stratosphere consist of a purely absorbing gray (spectrally flat) haze; this assumption provides a good fit to the data and we do not have enough spectral information to support a more complex haze model. Even with a gray haze, the haze location can affect the spectral shape and in the following section we discuss this effect on the retrieved abundances.

A very limited number of parameters are allowed to vary in these NEMESIS retrievals: the abundances of a subset of atmospheric gases (each via a single scaling factor applied to the a priori vertical profile) and the optical thickness of the stratospheric haze. The red line in Figure 1 shows the fit that was obtained for the equatorial spectrum using only three parameters: the C_2H_2 and C_2H_6 abundances and the opacity of an extended stratospheric haze layer. In this example fit, NH_3 and PH_3 were not included in the model. Even with such a limited parameter space, we are able to achieve a good fit to the data. In the following section, we perform retrievals on the 164–200 nm part of the spectrum, and therefore C_2H_6 absorption has no impact and is not allowed to vary. We initially allow only C_2H_2 and the haze opacity to vary, and then subsequently allow for NH_3 and PH_3 variability in order to confirm that they do not affect the qualitative results.

3.2. Latitudinal Retrievals

As shown in Melin et al. (2020), at wavelengths 164–200 nm, ultraviolet photons are primarily reflected from the 5–50 mbar region, with longer wavelengths probing slightly deeper in the atmosphere. Even though, we assume a spectrally flat haze, if the location of the haze intersects with this region of peak sensitivity, it is possible for the haze to affect the spectral shape. Instead, if we assume that the haze is located much higher in the atmosphere, well above the region of peak sensitivity, then increasing its opacity simply scales down the spectrum without impacting its shape. This in turn means that the spectral shape variability shown in Figure 2 is almost entirely due to C_2H_2 variability.

To explore this simple case, we performed retrievals at all latitudes in which only two parameters were allowed to vary: the scaling factor of the C_2H_2 vertical profile and the opacity of a compact haze layer located at 10 μbar, well above the region of peak sensitivity. The results of this retrieval are shown in orange in Figure 3. Figure 3a shows the C_2H_2 scaling factor, which is defined relative to the Moses et al. (2005) Model C vertical profile, i.e., a scaling factor of 1.0 is the same as the Moses et al. (2005) vertical profile while a scaling factor of 0.5 is half as abundant at all pressure levels. In Model C, the C_2H_2 density peaks at 0.55 mbar and it is therefore this part of the atmosphere that has the strongest influence on the C_2H_2 retrievals, although the spectrum is sensitive to the total column abundance down to the 5–50 mbar region.

As expected from Figure 2, the orange line in Figure 3a shows that the C_2H_2 abundance decreases rapidly at high latitudes; by ±60°, the abundance is approximately a quarter of the low-latitude value. Figure 3b shows the retrieved haze opacity, which increases toward the poles as expected and Figure 3c shows the reduced chi-square statistic, which shows that this simple two-parameter retrieval can achieve a good fit ($\chi^2 / n < 1$) at all latitudes.

If the haze is moved deeper in the atmosphere, into a region where it intersects with the region of peak sensitivity, then changing the haze opacity can also alter the spectral shape. As shown in Melin et al. (2020), the longer wavelength part of the spectrum probes slightly deeper in the atmosphere, both due to an absence of stratospheric absorbers and because of decreased Rayleigh scattering. A haze layer placed within the region of peak sensitivity therefore absorbs a higher fraction of the light at long wavelengths, since at shorter wavelengths, some of the sunlight is reflected before it reaches the haze layer. This can introduce a "tilt" in the spectrum, which can be compensated for by increasing the C_2H_2 abundance. In other words, this introduces a degeneracy between the haze opacity and the C_2H_2 abundance. This can be seen from the blue lines in Figure 3, which show the retrieval results when a compact haze layer at 5 mbar is used; toward the poles, where the opacity is higher, the blue line has a higher C_2H_2 abundance than the orange line. This is particularly true in the northern hemisphere, where the abundance ticks upward to reach the low-latitude levels. However, it should be noted that at these most northern latitudes, the 5 mbar haze model produces a worse fit to the data than the 10 μbar model, and continuing to move the compact haze deeper into the atmosphere continues to worsen the fit.

These two compact haze models represent the two extremes of the possible haze location; high enough that it does not overlap with the region of peak sensitivity and the deepest possible level that still allows for a good quality fit to the data. In reality, neither of these models is physically realistic, as the stratospheric haze is likely to be extended over a large pressure range. As there is haze opacity within the region of peak sensitivity and also at higher altitudes, the true C_2H_2 distribution likely lies between the blue and orange lines in Figure 3a. To explore this, we created an extended haze model with constant density in the 100–1 mbar range, approximated from the aerosol model described in Wong et al. (2003). The latitudinal retrieval results using this model are shown in green in Figure 3. As expected, the retrieved C_2H_2 abundances lie between the results from the other two models. In addition, the quality of the fit is better at almost all latitudes. We note that despite the very simple haze parameterization, the retrieved latitudinal haze opacities shown in Figure 3b are very similar to the asymmetric latitudinal haze distribution obtained by Zhang, West, et al. (2013) from Cassini ISS and ground-based near-infrared observations.

Thus far, our retrievals have been limited to C_2H_2 and the haze opacity, and tropospheric NH_3 and PH_3 have not been included in the atmospheric model. In order to understand the impact that they may have on the retrieved C_2H_2 distribution, we conducted another series of retrievals using the extended haze model where NH_3 and PH_3 were included and were also allowed to vary via a scaling parameter. This inclusion had minimal impact on the retrieved C_2H_2 abundances (although it does increase the error bars) and did not improve the quality of the fit to the data.

4. Discussion and Conclusions

In this study, we use ultraviolet reflected sunlight observations of Jupiter to determine how the planet's stratospheric C_2H_2 abundance varies with latitude. We performed latitudinal retrievals where we allowed the C_2H_2 abundance to vary via a scaling factor and found that this scaling factor peaks at low latitudes and decreases toward the poles. In these retrievals, we assume that all latitudes have the same relative vertical distribution of C_2H_2; in reality this may vary and the UVS data are not capable of vertically resolving the abundance profile. However, we carefully selected our Juno UVS data such that all of the latitudinal spectra have the same solar and observational geometry and therefore probe down to the same region of the atmosphere. The scaling factor is therefore representative of the total C_2H_2 abundance above the 5–50 mbar level. The precise latitudinal distribution depends on the assumptions made about the stratospheric haze altitude, but the high-latitude abundances are ~2–4 times lower than the equatorial abundances.

There have been several papers that have studied Jupiter's meridional distribution of C_2H_2 using infrared observations, from both spacecraft (Nixon et al., 2007, 2010; Zhang, Nixon, et al., 2013) and ground-based

Table 1
Comparison of Full-Planet Meridional C_2H_2 Studies

Year	Jupiter season	Data source	Meridional trend	Reference
1979	Northern fall	Voyager IRIS	Constant with latitude at 0.1–7 mbar	Nixon et al. (2010)
2000	Northern summer	Cassini CIRS	Decreases toward poles by a factor of ~4 at 5 mbar, clear north-south asymmetry (maximum at 20°N)	Nixon et al. (2007)
2014	Northern fall	IRTF TEXES	Decreases toward poles by a factor of ~2 at 5 mbar, some north-south asymmetry but less than in Cassini CIRS data	Fletcher et al. (2016)
2013–2017	Northern fall	IRTF TEXES	Decreases toward poles by factors of 2–3 at 1 mbar, north-south asymmetry decreases over 4 yr of observations, symmetric by 2017	Melin et al. (2018)
2016–2020	Northern winter	Juno UVS	Decreases toward poles by a factor of 2–4 at pressures less than 5–50 mbar, no clear north-south asymmetry	This article

telescopes (Fletcher et al., 2016; Melin et al., 2018). High resolution infrared observations have the advantage in being able to separate individual emission lines and can be used to retrieve the vertical profile of a molecular species. However, ultraviolet observations have the advantage that they are not dependent on the temperature profile in the stratosphere, a significant difficulty in infrared analyses (e.g., Fletcher et al., 2016). The results presented in this study are the first full-planet meridional retrievals of C_2H_2 from ultraviolet observations and they build on the work of Melin et al. (2020) which presents low-latitude retrievals from Cassini UVIS.

Table 1 describes the results from previous studies of Jupiter's meridional C_2H_2 distribution. The decrease of C_2H_2 by a factor of up to 4 at high latitudes is a trend that was seen in three of the four previous full-planet studies (Fletcher et al., 2016; Melin et al., 2018; Nixon et al., 2007). This clear agreement between observations from different spectral regions is reassuring. This result also agrees with the expectation from solar insolation rates; near the equator, the UV flux is higher, allowing more C_2H_2 to be generated from the UV photolysis of CH_4. Including the effect of horizontal mixing complicates this picture and can act to flatten the distribution. The horizontal mixing efficiency has previously been estimated by tracking the post-impact spread of SL9-related species over decades and by studying the hydrocarbon distribution using coupled chemistry-transport models; the constraints provided by these observations are limited in pressure and latitude, but assuming a reasonable range of horizontal mixing processes has been shown to still result in a decrease toward the poles in the C_2H_2 abundance (Hue et al., 2018).

The exception to this latitudinal trend is the reanalysis of Voyager IRIS data; while an earlier preliminary analysis suggested that C_2H_2 decreases at high latitude in the Voyager IRIS observations (Maguire et al., 1984), Nixon et al. (2010) reanalyzed the data using the same methods used for the Cassini CIRS data and found that the abundance was approximately constant with latitude (up to $\pm60°$). Nixon et al. (2010) suggested that this could be due to seasonal effects from Jupiter's eccentric orbit, although subsequent observations during the same season (northern fall) three Jovian years later (Fletcher et al., 2016; Melin et al., 2018) do show a decrease toward the poles and modeling work from Hue et al. (2018) shows that there should be minimal seasonal effects on the hydrocarbon abundances at these depths.

In addition to the high-latitude decrease, the studies listed in Table 1 also discuss the (a)symmetry of the meridional distribution at lower latitude. In 2000, Nixon et al. (2007) found that the peak C_2H_2 abundance was at 20°N rather than at the equator. Fletcher et al. (2016) observed a similar asymmetry in 2014 and Melin et al. (2018) observed that this asymmetry decreased over the 2013–2017 time period. Melin et al. (2018) suggested that the cause for this asymmetry could be related to periods of strong wave activity in Jupiter's Northern Equatorial Belt or other dynamic tropospheric events that might lead to material or wave transfer of energy with altitude. Our observations in this study were obtained during 2016–2020 and do not show any strong north-south asymmetry within the low-latitude region. The individual latitudinal distributions shown in Figure 3 indicate some asymmetries at high latitudes, but when we consider all four model runs together, this asymmetry falls within the error bars.

In this study, we focused exclusively on meridional trends, and we excluded auroral regions from the highest-latitude spectra, due to the complexity of analyzing spectra that combine auroral emission and

reflected sunlight. The meridional infrared studies we discuss similarly avoided regions of the planet with auroral emission (Melin et al., 2018; Nixon et al., 2007). However, within the polar region of the planet, the hydrocarbon distribution appears to vary strongly with latitude; using infrared observations, Sinclair et al. (2017, 2018) found that there is an enrichment in C_2H_2 within the auroral ovals, relative to the surrounding quiescent longitudes. As a polar-orbiting spacecraft, Juno provides excellent views of Jupiter's poles. In the future, we will therefore seek to expand this study and use Juno UVS observations to map the polar C_2H_2 distribution.

Data Availability Statement

The Juno UVS data used in this study are archived in NASA's Planetary Data System Atmospheres Node: https://pds-atmospheres.nmsu.edu/PDS/data/jnouvs_3001 (Trantham, 2014). The data used to produce the figures in this study are available in Giles (2021). The NEMESIS radiative transfer and retrieval tool is available from Irwin (2020).

References

Bétremieux, Y., & Yelle, R. V. (1999). HST detection of H_2 Raman scattering in the Jovian atmosphere. *Icarus*, *142*(2), 324–341. https://doi.org/10.1006/icar.1999.6217

Bolton, S. J., Lunine, J., Stevenson, D., Connerney, J. E. P., Levin, S., Owen, T. C., et al. (2017). The Juno mission. *Space Science Reviews*, *213*(1–4), 5–37. https://doi.org/10.1007/978-94-024-1560-5_2

Bonfond, B., Saur, J., Grodent, D., Badman, S. V., Bisikalo, D., Shematovich, V., et al. (2017). The tails of the satellite auroral footprints at Jupiter. *Journal of Geophysical Research: Space Physics*, *122*(8), 7985–7996. https://doi.org/10.1002/2017ja024370

Drossart, P., Bézard, B., Atreya, S. K., Lacy, J., Serabyn, E., Tokunaga, A., & Encrenaz, T. (1986). Enhanced acetylene emission near the north pole of Jupiter. *Icarus*, *66*(3), 610–618. https://doi.org/10.1016/0019-1035(86)90094-1

Fletcher, L. N., Greathouse, T. K., Orton, G. S., Sinclair, J. A., Giles, R. S., Irwin, P. G. J., & Encrenaz, T. (2016). Mid-infrared mapping of Jupiter's temperatures, aerosol opacity and chemical distributions with IRTF/TEXES. *Icarus*, *278*, 128–161. https://doi.org/10.1016/j.icarus.2016.06.008

Fletcher, L. N., Orton, G. S., de Pater, I., Edwards, M. L., Yanamandra-Fisher, P. A., Hammel, H. B., et al. (2011). The aftermath of the July 2009 impact on Jupiter: Ammonia, temperatures, and particulates from Gemini thermal infrared spectroscopy. *Icarus*, *211*(1), 568–586. https://doi.org/10.1016/j.icarus.2010.09.012

Fouchet, T., Lellouch, E., Bézard, B., Feuchtgruber, H., Drossart, P., & Encrenaz, T. (2000). Jupiter's hydrocarbons observed with ISO-SWS: Vertical profiles of C_2H_6 and C_2H_2, detection of CH_3C_2H. *Astronomy & Astrophysics*, *355*, L13–L17.

Giles, R. S. (2021). *Meridional variations of C2H2 in Jupiter's stratosphere from Juno UVS observations* (Vol. 2). Mendeley Data. https://doi.org/10.17632/32txrwstzt.2

Gladstone, G. R., Persyn, S. C., Eterno, J. S., Walther, B. C., Slater, D. C., Davis, M. W., et al. (2017). The ultraviolet spectrograph on NASA's Juno mission. *Space Science Reviews*, *213*(1–4), 447–473. https://doi.org/10.1007/s11214-014-0040-z

Gladstone, G. R., & Yung, Y. L. (1983). An analysis of the reflection spectrum of Jupiter from 1500 to 1740 Å. *The Astrophysical Journal*, *266*(1), 415–424. https://doi.org/10.1086/160789

Hue, V., Hersant, F., Cavalié, T., Dobrijevic, M., & Sinclair, J. (2018). Photochemistry, mixing, and transport in Jupiter's stratosphere constrained by Cassini. *Icarus*, *307*, 106–123. https://doi.org/10.1016/j.icarus.2018.02.018

Irwin, P. G. J. (2020). *NEMESIS/Radtrancode software (Version 1.0)*. Zenodo. https://doi.org/10.5281/zenodo.4303976

Irwin, P. G. J., Teanby, N. A., de Kok, R., Fletcher, L. N., Howett, C. J. A., Tsang, C. C. C., et al. (2008). The NEMESIS planetary atmosphere radiative transfer and retrieval tool. *Journal of Quantitative Spectroscopy and Radiative Transfer*, *109*(6), 1136–1150. https://doi.org/10.1016/j.jqsrt.2007.11.006

Kammer, J. A., Hue, V., Greathouse, T. K., Gladstone, G. R., Davis, M. W., & Versteeg, M. H. (2019). Planning operations in Jupiter's high-radiation environment: Optimization strategies from Juno-ultraviolet spectrograph. *Journal of Astronomical Telescopes, Instruments, and Systems*, *5*(2), 027001. https://doi.org/10.1117/1.jatis.5.2.027001

Kim, S. J., Caldwell, J., Rivolo, A. R., Wagener, R., & Orton, G. S. (1985). Infrared polar brightening on Jupiter: III. Spectrometry from the Voyager 1 IRIS experiment. *Icarus*, *64*(2), 233–248. https://doi.org/10.1016/0019-1035(85)90088-0

Kostiuk, T., Buhl, D., Espenak, F., Romani, P., Bjoraker, G., Fast, K., et al. (1996). Stratospheric ammonia on Jupiter after the SL9 collision. *Icarus*, *121*(2), 431–441. https://doi.org/10.1006/icar.1996.0098

Kunde, V. G., Flasar, F. M., Jennings, D. E., Bézard, B., Strobel, D. F., Conrath, B. J., et al. (2004). Jupiter's atmospheric composition from the Cassini thermal infrared spectroscopy experiment. *Science*, *305*(5690), 1582–1586. https://doi.org/10.1126/science.1100240

Lellouch, E., Bézard, B., Strobel, D. F., Bjoraker, G. L., Flasar, F. M., & Romani, P. N. (2006). On the HCN and CO_2 abundance and distribution in Jupiter's stratosphere. *Icarus*, *184*(2), 478–497. https://doi.org/10.1016/j.icarus.2006.05.018

Maguire, W. C., Samuelson, R. E., Hanel, R. A., & Kunde, V. G. (1984). Latitudinal variation of acetylene and ethane in the Jovian atmosphere from Voyager IRIS observations. *Bulletin of the American Astronomical Society*, *16*, 647.

Melin, H., Fletcher, L. N., Donnelly, P. T., Greathouse, T. K., Lacy, J. H., Orton, G. S., et al. (2018). Assessing the long-term variability of acetylene and ethane in the stratosphere of Jupiter. *Icarus*, *305*(1), 301–313. https://doi.org/10.1016/j.icarus.2017.12.041

Melin, H., Fletcher, L. N., Irwin, P. G. J., & Edgington, S. G. (2020). Jupiter in the ultraviolet: Acetylene and ethane abundances in the stratosphere of Jupiter from Cassini observations between 0.15 and 0.19 m. *The Astronomical Journal*, *159*(6), 291. https://doi.org/10.3847/1538-3881/ab91a6

Morrissey, P. F., Feldman, P. D., McGrath, M. A., Wolven, B. C., & Moos, H. W. (1995). The ultraviolet reflectivity of Jupiter at 3.5 Å resolution from Astro-1 and Astro-2. *Astrophysical Journal Letters*, *454*(1), L65. https://doi.org/10.1086/309763

Moses, J. I., Fouchet, T., Bézard, B., Gladstone, G. R., Lellouch, E., & Feuchtgruber, H. (2005). Photochemistry and diffusion in Jupiter's stratosphere: Constraints from ISO observations and comparisons with other giant planets. *Journal of Geophysical Research: Planets*, *110*(E8), E08001. https://doi.org/10.1029/2005je002411

Moses, J. I., Fouchet, T., Yelle, R. V., Friedson, A. J., Orton, G. S., Bézard, B., & et al. (2004). The stratosphere of Jupiter. In F. Bagenal, T. E. Dowling, W. B. McKinnon (Eds.), *Jupiter: The planet, satellites and magnetosphere*. Cambridge University Press.

Nixon, C. A., Achterberg, R. K., Conrath, B. J., Irwin, P. G. J., Teanby, N. A., Fouchet, T., et al. (2007). Meridional variations of C_2H_2 and C_2H_6 in Jupiter's atmosphere from Cassini CIRS infrared spectra. *Icarus*, *188*(1), 47–71. https://doi.org/10.1016/j.icarus.2006.11.016

Nixon, C. A., Achterberg, R. K., Romani, P. N., Allen, M., Zhang, X., Teanby, N. A., et al. (2010). Abundances of Jupiter's trace hydrocarbons from Voyager and Cassini. *Planetary and Space Science*, *58*(13), 1667–1680. https://doi.org/10.1016/j.pss.2010.05.008

Plass, G. N., Kattawar, G. W., & Catchings, F. E. (1973). Matrix operator theory of radiative transfer. 1: Rayleigh scattering. *Applied Optics*, *12*(2), 314–329. https://doi.org/10.1364/ao.12.000314

Ridgway, S. T. (1974). Jupiter: Identification of ethane and acetylene. *The Astrophysical Journal*, *187*, L41–L43. https://doi.org/10.1086/181388

Rodgers, C. D. (2000). *Inverse methods for atmospheric sounding: Theory and practice*. World Scientific.

Sada, P. V., Bjoraker, G. L., Jennings, D. E., McCabe, G. H., & Romani, P. N. (1998). Observations of CH_4, C_2H_6, and C_2H_2 in the stratosphere of Jupiter. *Icarus*, *136*(2), 192–201. https://doi.org/10.1006/icar.1998.6021

Sinclair, J. A., Moses, J. I., Hue, V., Greathouse, T. K., Orton, G. S., Fletcher, L. N., & Irwin, P. G. J. (2019). Jupiter's auroral-related stratospheric heating and chemistry III: Abundances of C_2H_4, CH_3C_2H, C_4H_2, and C_6H_6 from Voyager-IRIS and Cassini-CIRS. *Icarus*, *328*, 176–193. https://doi.org/10.1016/j.icarus.2019.03.012

Sinclair, J. A., Orton, G. S., Fletcher, L. N., Roman, M., de Pater, I., Encrenaz, T., et al. (2020). Spatial structure in Neptune's 7.90 μm stratospheric CH_4 emission, as measured by VLT-VISIR. *Icarus*, *345*, 113748. https://doi.org/10.1016/j.icarus.2020.113748

Sinclair, J. A., Orton, G. S., Greathouse, T. K., Fletcher, L. N., Moses, J. I., Hue, V., & Irwin, P. G. J. (2017). Jupiter's auroral-related stratospheric heating and chemistry I: Analysis of Voyager-IRIS and Cassini-CIRS spectra. *Icarus*, *292*, 182–207. https://doi.org/10.1016/j.icarus.2016.12.033

Sinclair, J. A., Orton, G. S., Greathouse, T. K., Fletcher, L. N., Moses, J. I., Hue, V., & Irwin, P. G. J. (2018). Jupiter's auroral-related stratospheric heating and chemistry II: Analysis of IRTF-TEXES spectra measured in December 2014. *Icarus*, *300*, 305–326. https://doi.org/10.1016/j.icarus.2017.09.016

Trantham, B. (2014). *JNO-J-UVS-3-RDR-V1.0*. NASA Planetary Data System.

Wong, A.-S., Lee, A. Y. T., Yung, Y. L., & Ajello, J. M. (2000). Jupiter: Aerosol chemistry in the polar atmosphere. *The Astrophysical Journal Letters*, *534*(2), L215–L217. https://doi.org/10.1086/312675

Wong, A.-S., Yung, Y. L., & Friedson, A. J. (2003). Benzene and haze formation in the polar atmosphere of Jupiter. *Geophysical Research Letters*, *30*(8). https://doi.org/10.1029/2002gl016661

Zhang, X., Nixon, C. A., Shia, R. L., West, R. A., Irwin, P. G. J., Yelle, R. V., et al. (2013). Radiative forcing of the stratosphere of Jupiter, part I: Atmospheric cooling rates from Voyager to Cassini. *Planetary and Space Science*, *88*, 3–25. https://doi.org/10.1016/j.pss.2013.07.005

Zhang, X., West, R. A., Banfield, D., & Yung, Y. L. (2013). Stratospheric aerosols on Jupiter from Cassini observations. *Icarus*, *226*(1), 159–171. https://doi.org/10.1016/j.icarus.2013.05.020